PAPER • OPEN ACCESS

Overview of ASDEX upgrade results in view of ITER and DEMO

To cite this article: H. Zohm *et al* 2024 *Nucl. Fusion* **64** 112001

OPEN ACCESS
IOP Publishing | International Atomic Energy Agency Nuclear Fusion
Nucl. Fusion **64** (2024) 112001 (15pp) https://doi.org/10.1088/1741-4326/ad249d

Overview of ASDEX upgrade results in view of ITER and DEMO

H. Zohm[1,*], E. Alessi[12], C. Angioni[1], N. Arden[1], V. Artigues[1], M. Astrain[1], O. Asunta[4], M. Balden[1], V. Bandaru[1], A. Banon Navarro[1], M. Bauer[1], A. Bergmann[1], M. Bergmann[1], J. Bernardo[3], M. Bernert[1], A. Biancalani[42], R. Bielajew[41], R. Bilato[1], G. Birkenmeier[1,7], T. Blanken[5], V. Bobkov[1], A. Bock[1], L. Bock[1], T. Body[1], T. Bolzonella[8], N. Bonanomi[1], A. Bortolon[32], B. Böswirth[1], C. Bottereau[9], A. Bottino[1], H. van den Brand[5], M. Brenzke[10], S. Brezinsek[10], D. Brida[1], F. Brochard[11], J. Buchanan[6], A. Buhler[1], A. Burckhart[1], Y. Camenen[51], B. Cannas[38], P. Cano Megías[1], D. Carlton[1], M. Carr[6], P. Carvalho[3], C. Castaldo[50], A. Castillo Castillo[1], A. Cathey[1], M. Cavedon[44], C. Cazzaniga[8], C. Challis[6], A. Chankin[1], A. Chomiczewska[16], C. Cianfarani[50], F. Clairet[9], S. Coda[13], R. Coelho[3], J.W. Coenen[10], L. Colas[9], G. Conway[1], S. Costea[14], D. Coster[1], T. Cote[46], A.J. Creely[41], G. Croci[12], D.J. Cruz Zabala[20], G. Cseh[15], I. Cziegler[30], O. D'Arcangelo[34], A. Dal Molin[44], P. David[1], C. Day[17], M. de Baar[5], P. de Marné[1], R. Delogu[8], P. Denner[10], A. Di Siena[1], M. Dibon[1], J.J. Dominguez-Palacios Durán[20], D. Dunai[15], M. Dreval[52], M. Dunne[1], B.P. Duval[13], R. Dux[1], T. Eich[1], S. Elgeti[1], A. Encheva[43], B. Esposito[50], E. Fable[1], M. Faitsch[1], D. Fajardo Jimenez[1], U. Fantz[1], M. Farnik[45], H. Faugel[1], F. Felici[13], O. Ficker[45], A. Figueredo[3], R. Fischer[1], O. Ford[2], L. Frassinetti[18], M. Fröschle[1], G. Fuchert[2], J.C. Fuchs[1], H. Fünfgelder[1], S. Futatani[33], K. Galazka[16], J. Galdon-Quiroga[20], D. Gallart Escolà[33], A. Gallo[9], Y. Gao[10], S. Garavaglia[12], M. Garcia Muñoz[20], B. Geiger[46], L. Giannone[1], S. Gibson[49], L. Gil[3], E. Giovannozzi[50], I. Girka[1], O. Girka[1], T. Gleiter[1], S. Glöggler[1,7], M. Gobbin[8], J.C. Gonzalez[1], J. Gonzalez Martin[20], T. Goodman[13], G. Gorini[44], T. Görler[1], D. Gradic[2], G. Granucci[12], A. Gräter[1], G. Grenfell[1], H. Greuner[1], M. Griener[1], M. Groth[4], O. Grover[1], A. Gude[1], L. Guimarais[3], S. Günter[1], D. Hachmeister[3], A.H. Hakola[21], C. Ham[6], T. Happel[1], N. den Harder[1], G. Harrer[29], J. Harrison[6], V. Hauer[17], T. Hayward-Schneider[1], B. Heinemann[1], P. Heinrich[1], T. Hellsten[19], S. Henderson[6], P. Hennequin[23], M. Herschel[1], S. Heuraux[11], A. Herrmann[1], E. Heyn[53], F. Hitzler[1,7], J. Hobirk[1], K. Höfler[2], S. Hörmann[1], J.H. Holm[25], M. Hölzl[1], C. Hopf[1], L. Horvath[30], T. Höschen[1], A. Houben[11], A. Hubbard[41], A. Huber[10], K. Hunger[1], V. Igochine[1], M. Iliasova[40], J. Illerhaus[1], K. Insulander Björk[47], C. Ionita-Schrittwieser[14], I. Ivanova-Stanik[16], S. Jachmich[43], W. Jacob[1], N. Jaksic[1], A. Jansen van Vuuren[20], F. Jaulmes[45], F. Jenko[1], T. Jensen[25], E. Joffrin[9], A. Kallenbach[1], J. Kalis[1], A. Kappatou[1], J. Karhunen[4], C.-P. Käsemann[1], S. Kasilov[53,54], Y. Kazakov[28], A. Kendl[14], W. Kernbichler[29], E. Khilkevitch[40], M. Kircher[1], A. Kirk[6], S. Kjer Hansen[41], V. Klevarova[27], F. Klossek[1], G. Kocsis[15], M. Koleva[1], M. Komm[45], M. Kong[13], A. Krämer-Flecken[10], M. Krause[1], I. Krebs[5], A. Kreuzeder[1], K. Krieger[1], O. Kudlacek[1], D. Kulla[2], T. Kurki-Suonio[4], B. Kurzan[1], B. Labit[13], K. Lackner[1], F. Laggner[32], A. Lahtinen[4], P. Lainer[29], P.T. Lang[1], P. Lauber[1], M. Lehnen[43], L. Leppin[1], E. Lerche[1], N. Leuthold[19], L. Li[10], J. Likonen[21], O. Linder[1], H. Lindl[1], B. Lipschultz[30], Y. Liu[19], Z. Lu[1], T. Luda Di Cortemiglia[1], N.C. Luhmann[31],

[a] See the author list of 'Overview of the EUROfusion Tokamak Exploitation Programme in Support of ITEER and DEMO' by E. Joffrin et al to be published in Nuclear Fusion Special Issue: Overview and Summary Papers from the 29th Fusion Energy Conference (London, UK, 16-21 October 2023).
[b] See Zohm *et al* 2024 (https://doi.org/10.1088/1741-4326/ad249d) for the ASDEX Upgrade Team.
[*] Author to whom any correspondence should be addressed.

T. Lunt[1], A. Lyssoivan[28], T. Maceina[1], J. Madsen[25], A. Magnanimo[1], H. Maier[1], J. Mailloux[6], R. Maingi[32], O. Maj[1], E. Maljaars[5], V. Maquet[28], A. Mancini[12], A. Manhard[1], P. Mantica[12], M. Mantsinen[33,56], P. Manz[55], M. Maraschek[1], C. Marchetto[37], M. Markl[29], L. Marrelli[8], P. Martin[8], F. Matos[1], M. Mayer[1], P.J. McCarthy[35], R. McDermott[1], G. Meng[1], R. Merkel[1], A. Merle[13], H. Meyer[6], M. Michelini[1], D. Milanesio[37], V. Mitterauer[1], P. Molina Cabrera[1], M. Muraca[1], F. Nabais[3], V. Naulin[25], R. Nazikian[32], R.D. Nem[25], R. Neu[1,36], A.H. Nielsen[25], S.K. Nielsen[25], T. Nishizawa[1], M. Nocente[44], I. Novikau[1], S. Nowak[12], R. Ochoukov[1], J. Olsen[25], P. Oyola[20], O. Pan[1], G. Papp[1], A. Pau[13], G. Pautasso[1], C. Paz-Soldan[19], M. Peglau[1], E. Peluso[26], P. Petersson[18], C. Piron[8], U. Plank[1], B. Plaum[24], B. Plöckl[1], V. Plyusnin[3], G. Pokol[15,22], E. Poli[1], A. Popa[1], L. Porte[13], J. Puchmayr[1], T. Pütterich[1], L. Radovanovic[29], M. Ramisch[24], J. Rasmussen[25], G. Ratta[48], S. Ratynskaia[18], G. Raupp[1], A. Redl[54], D. Réfy[15], M. Reich[1], F. Reimold[2], D. Reiser[10], M. Reisner[1], D. Reiter[10], B. Rettino[1], T. Ribeiro[1], D. Ricci[12], R. Riedl[1], J. Riesch[1], J.F. Rivero Rodriguez[20], G. Rocchi[50], P. Rodriguez-Fernandez[41], V. Rohde[1], G. Ronchi[5], M. Rott[1], M. Rubel[18], D.A. Ryan[6], F. Ryter[1], S. Saarelma[6], M. Salewski[25], A. Salmi[4], O. Samoylov[1], L. Sanchis Sanchez[20], J. Santos[3], O. Sauter[13], G. Schall[1], A. Schlüter[1], J. Scholte[5], K. Schmid[1], O. Schmitz[46], P.A. Schneider[1], R. Schrittwieser[14], M. Schubert[1], C. Schuster[1], N. Schwarz[1], T. Schwarz-Selinger[1], J. Schweinzer[1], F. Sciortino[1], O. Seibold-Benjak[1], A. Shabbir[27], A. Shalpegin[13], S. Sharapov[6], U. Sheikh[13], A. Shevelev[40], G. Sias[38], M. Siccinio[1], B. Sieglin[1], A. Sigalov[1], A. Silva[3], C. Silva[3], D. Silvagni[1], J. Simpson[6], S. Sipilä[4], A. Snicker[4], E. Solano[48], C. Sommariva[13], C. Sozzi[12], M. Spacek[1], G. Spizzo[8], M. Spolaore[8], A. Stegmeir[1], M. Stejner[25], D. Stieglitz[1], J. Stober[1], U. Stroth[1,7], E. Strumberger[1], G. Suarez Lopez[1], W. Suttrop[1], T. Szepesi[15], B. Tál[1], T. Tala[21], W. Tang[1], G. Tardini[1], M. Tardocchi[12], D. Terranova[8], M. Teschke[1], E. Thorén[18], W. Tierens[1], D. Told[1], W. Treutterer[1], G. Trevisan[8], M. Tripský[28], P. Ulbl[1], G. Urbanczyk[1], M. Usoltseva[1], M. Valisa[8], M. Valovic[6], S. van Mulders[13,43], M. van Zeeland[19], F. Vannini[1], B. Vanovac[41], P. Varela[3], S. Varoutis[17], T. Verdier[25], G. Verdoolaege[27,28], N. Vianello[8], J. Vicente[3], T. Vierle[1], E. Viezzer[20], I. Voitsekhovitch[6], U. von Toussaint[1], D. Wagner[1], X. Wang[1], M. Weiland[1], D. Wendler[1,7], A.E. White[41], M. Willensdorfer[1], B. Wiringer[1], M. Wischmeier[1], R. Wolf[2], E. Wolfrum[1], Q. Yang[39], C. Yoo[41], Q. Yu[1], R. Zagórski[16], I. Zammuto[1], T. Zehetbauer[1], W. Zhang[39], W. Zholobenko[1], A. Zibrov[1], M. Zilker[1], C.F.B. Zimmermann[1,7], A. Zito[1], H. Zohm[1], S. Zoletnik[15], the EUROfusion Tokamak Exploitation Team[a] and the ASDEX Upgrade Team[b]

[1] Max-Planck-Institut für Plasmaphysik, Garching, Germany
[2] Max-Planck-Institut für Plasmaphysik, Greifswald, Germany
[3] Instituto de Plasmas e Fusão Nuclear, Instituto Superior Técnico, Universidade de Lisboa, Lisbon, Portugal
[4] Department of Applied Physics, Aalto University, Helsinki, Finland
[5] Eindhoven, University of Technology, Eindhoven, Netherlands
[6] CCFE, Culham Science Centre, Abingdon, United Kingdom of Great Britain and Northern Ireland
[7] Physik-Department E28, Technische Universität München, Garching, Germany
[8] Consorzio RFX, Padova, Italy
[9] CEA/IRFM, Saint Paul Lez Durance, France
[10] Forschungszentrum, Jülich, Germany
[11] Institut Jean Lamour, Université de Lorraine, Nancy, France
[12] ENEA, IFP-CNR, Milan, Italy
[13] Ecole Polytechnique Fédérale de Lausanne (EPFL), Swiss Plasma Center (SPC), Lausanne, Switzerland
[14] ÖAW, IAP, University of Innsbruck, Innsbruck, Austria
[15] Centre for Energy Research, Budapest, Hungary
[16] Institute of Plasma Physics and Laser Microfusion, Warsaw, Poland
[17] Karlsruhe Institut für Technologie, Karlsruhe, Germany
[18] KTH Royal Institute of Technology, Stockholm, Sweden
[19] General Atomics, San Diego, CA, United States of America
[20] Universidad de Sevilla, Sevilla, Spain

[21] VTT Technical Research Centre of Finland, Helsinki, Finland
[22] Budapest University of Technology and Economics, Budapest, Hungary
[23] Laboratoire de Physique des Plasmas, Ecole Polytechnique, Palaiseau, France
[24] IGVP Universität Stuttgart, Stuttgart, Germany
[25] Department of Physics, Technical University of Denmark, Kgs. Lyngby, Denmark
[26] Department of Industrial Engineering, University of Rome, Rome, Italy
[27] Ghent University, Ghent, Belgium
[28] ERM/KMS, Brussels, Belgium
[29] ÖAW, IAP, Vienna University of Technology, Vienna, Austria
[30] York Plasma Institute, University of York, York, United Kingdom of Great Britain and Northern Ireland
[31] Electrical and Computer Engineering, University of California, Davis, CA, United States of America
[32] Princeton Plasma Physics Laboratory, Princeton, NJ, United States of America
[33] Barcelona Supercomputing Center, Barcelona, Spain
[34] ENEA Consorzio CREATE, Naples, Italy
[35] School of Physics, University College Cork, Cork, Ireland
[36] Technische Universität München, Garching, Germany
[37] ISC-CNR and Politecnico di Torino, Torino, Italy
[38] Department of Electrical and Electronic Engineering, University of Cagliari, Cagliari, Italy
[39] Chinese Academy of Sciences, Hefei, China
[40] Ioffe Institute, St. Petersburg, Russian Federation
[41] MIT Plasma Science and Fusion Center, Cambridge, MA, United States of America
[42] Modeling Group, École supérieure d'ingénieurs Léonard-de-Vinci, Courbevoie, France
[43] ITER Organization, Saint-Paul-lez-Durance, France
[44] ENEA, University of Milano-Bicocca, Milano, Italy
[45] Institute of Plasma Physics of the CAS, Praha, Czech Republic
[46] University of Wisconsin, Madison, WI, United States of America
[47] Department of Physics, Chalmers University of Technology, Gothenburg, Sweden
[48] Laboratorio Nacional de Fusión, CIEMAT, Madrid, Spain
[49] Department of Physics, Durham University, Durham, United Kingdom of Great Britain and Northern Ireland
[50] ENEA, Centro Ricerche Frascati, Frascati, Italy
[51] Aix-Marseille University, CNRS, Marseille, France
[52] Institute of Plasma Physics, National Science Center Kharkov Institute of Physics and Technology, Krakov, Ukraine
[53] ÖAW, Graz University of Technology, Graz, Austria
[54] Universitá degli Studi della Tuscia, DEIM Department, Viterbo, Italy
[55] Universität Greifswald, Greifswald, Germany
[56] ICREA, Barcelona, Spain

E-mail: hartmut.zohm@ipp.mpg.de

Received 23 November 2023, revised 4 January 2024
Accepted for publication 31 January 2024
Published 19 August 2024

Abstract

Experiments on ASDEX Upgrade (AUG) in 2021 and 2022 have addressed a number of critical issues for ITER and EU DEMO. A major objective of the AUG programme is to shed light on the underlying physics of confinement, stability, and plasma exhaust in order to allow reliable extrapolation of results obtained on present day machines to these reactor-grade devices. Concerning pedestal physics, the mitigation of edge localised modes (ELMs) using resonant magnetic perturbations (RMPs) was found to be consistent with a reduction of the linear peeling-ballooning stability threshold due to the helical deformation of the plasma. Conversely, ELM suppression by RMPs is ascribed to an increased pedestal transport that keeps the plasma away from this boundary. Candidates for this increased transport are locally enhanced turbulence and a locked magnetic island in the pedestal. The enhanced D-alpha (EDA) and quasi-continuous exhaust (QCE) regimes have been established as promising ELM-free scenarios. Here, the pressure gradient at the foot of the H-mode pedestal is reduced by a quasi-coherent mode, consistent with violation of the high-n ballooning mode stability limit there. This is suggestive that the EDA and QCE regimes have a common underlying physics

origin. In the area of transport physics, full radius models for both L- and H-modes have been developed. These models predict energy confinement in AUG better than the commonly used global scaling laws, representing a large step towards the goal of predictive capability. A new momentum transport analysis framework has been developed that provides access to the intrinsic torque in the plasma core. In the field of exhaust, the X-Point Radiator (XPR), a cold and dense plasma region on closed flux surfaces close to the X-point, was described by an analytical model that provides an understanding of its formation as well as its stability, i.e., the conditions under which it transitions into a deleterious MARFE with the potential to result in a disruptive termination. With the XPR close to the divertor target, a new detached divertor concept, the compact radiative divertor, was developed. Here, the exhaust power is radiated before reaching the target, allowing close proximity of the X-point to the target. No limitations by the shallow field line angle due to the large flux expansion were observed, and sufficient compression of neutral density was demonstrated. With respect to the pumping of non-recycling impurities, the divertor enrichment was found to mainly depend on the ionisation energy of the impurity under consideration. In the area of MHD physics, analysis of the hot plasma core motion in sawtooth crashes showed good agreement with nonlinear 2-fluid simulations. This indicates that the fast reconnection observed in these events is adequately described including the pressure gradient and the electron inertia in the parallel Ohm's law. Concerning disruption physics, a shattered pellet injection system was installed in collaboration with the ITER International Organisation. Thanks to the ability to vary the shard size distribution independently of the injection velocity, as well as its impurity admixture, it was possible to tailor the current quench rate, which is an important requirement for future large devices such as ITER. Progress was also made modelling the force reduction of VDEs induced by massive gas injection on AUG. The H-mode density limit was characterised in terms of safe operational space with a newly developed active feedback control method that allowed the stability boundary to be probed several times within a single discharge without inducing a disruptive termination. Regarding integrated operation scenarios, the role of density peaking in the confinement of the ITER baseline scenario (high plasma current) was clarified. The usual energy confinement scaling ITER98(p,y) does not capture this effect, but the more recent H20 scaling does, highlighting again the importance of developing adequate physics based models. Advanced tokamak scenarios, aiming at large non-inductive current fraction due to non-standard profiles of the safety factor in combination with high normalised plasma pressure were studied with a focus on their access conditions. A method to guide the approach of the targeted safety factor profiles was developed, and the conditions for achieving good confinement were clarified. Based on this, two types of advanced scenarios ('hybrid' and 'elevated' q-profile) were established on AUG and characterised concerning their plasma performance.

Keywords: tokamak, MHD stability, transport modelling, radiative exhaust, disruption physics, ELM free scenarios

(Some figures may appear in colour only in the online journal)

1. Introduction

The ASDEX Upgrade (AUG) [1] programme aims to resolve critical physics questions for ITER operation and the development of plasma scenarios for EU DEMO. The AUG plasma ($R_0 = 1.65$ m, $a = 0.5$ m, $I_p \leqslant 1.4$ MA, $B_t \leqslant 3.2$ T) is heated by up to 20 MW of NBI, 6 MW ECRH and 5 MW ICRH, supporting a wide range of plasma scenarios. The plasma is diagnosed by an extensive set of diagnostics and controlled by a discharge control system (DCS) that is constantly evolved to increase the possibilities of real-time control of plasma quantities. This also includes the development of the Fenix flight simulator combining a plasma model with models of the AUG sensors, actuators, and the DCS to design and test AUG discharges before execution, as well as to develop new controllers offline with short turn-around time [2]. Starting in 2007, the AUG first wall has been covered completely by tungsten (W), and the operational experience gained since then is now becoming very important for the ongoing discussions on the exchange of the ITER main chamber plasma facing material from Beryllium to Tungsten. As in previous years, up to 40% of the AUG programme have been conducted in the framework of the EUROfusion work package on tokamak exploitation (WPTE). A general overview of results obtained by WPTE can be found in [3].

New technical capabilities added in 2021/2022 include a shattered pellet injection (SPI) system funded by the ITER Organisation [4] and a 'variable gap' system for one of the NBI sources [5], which allows the acceleration gap to be adjusted between discharges, so that the injected power at

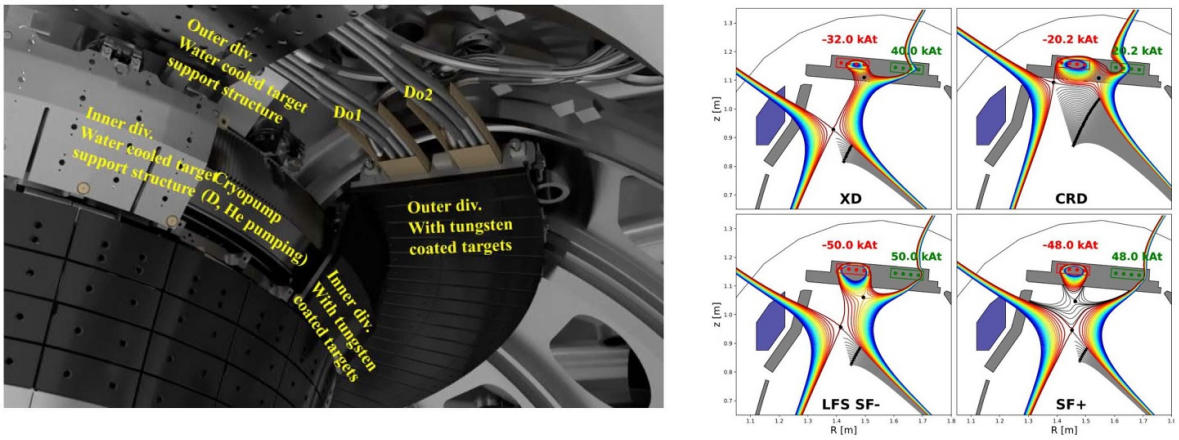

Figure 1. The new ASDEX Upgrade upper divertor consists of flat W-coated target tiles, a cryopump and two in-vessel coils (all shown in a CAD drawing in the left panel) that enable a variety of magnetic divertor configurations (right, XD = X-divertor, CRD = compact radiative divertor, LFS SF—= snowflake minus on the low field side, SF+ = snowflake plus).

low accelerating voltage can be increased. Despite Corona restrictions, e.g. limitation on the number of persons present in the control room, AUG operated regularly in 2021 and 2022, obtaining the wealth of results reported here. At present, the machine is in shutdown to install a new upper divertor, which will be used to explore advanced configurations for power and particle handling. The upgrade consists of two new in-vessel coils as shown in the left panel of figure 1, as well as new flat targets to increase the power handling capability and a cryopump to guarantee adequate pumping [6, 7]. With the new coils, a variety of non-standard magnetic configurations will be possible, as shown in the right panel of figure 1. The lower divertor will be kept unchanged in order to allow continuation of exhaust studies in ITER geometry. Operation is expected to resume in the second half of 2024.

2. Pedestal and edge physics

An important element for future reactor-grade tokamaks is the combination of the benefit of an H-mode pedestal with a benign exhaust scheme, avoiding large edge localised mode (ELM) bursts. ITER foresees to achieve this by suppressing ELMs using resonant magnetic perturbations (RMPs). While this method is also considered for the EU DEMO plasma scenario, several H-mode variants without large ELMs are also considered as candidates for this device. Both approaches are studied in AUG. Since the ITER and DEMO edge conditions (low pedestal top collisionality and high separatrix Greenwald fraction) cannot be reached simultaneously in present day devices, the AUG programme focused strongly on understanding the underlying physics. A key element is to understand, for the different stationary ELM-free regimes, what causes the increased pedestal transport that keeps the plasma away from the peeling-ballooning stability boundary without causing a back-transition to L-mode.

Concerning the suppression of ELMs by RMPs, the previously reported boundary for ELM mitigation [8], i.e. an increase in ELM frequency with simultaneous reduction of the energy per ELM crash, was found to be consistent with the lowering of the linear pedestal stability due to the 3-D deformation of the edge introduced by the RMP field [9]. Conversely, full ELM suppression is due to a reduction of pedestal pressure below the ideal MHD stability limit. This reduction is mainly due to the reduction of pedestal top density when applying RMPs and has partly been ascribed to increased turbulent particle transport in the presence of the RMP field [10]. A new study, employing a novel analysis technique using ECE data, identifies a locked magnetic island at the pedestal top during the suppression phase [11]. The signature of this magnetic island is not straightforward to detect by a phase jump in the ECE perturbation (as is the case for a large tearing mode in an otherwise axisymmetric plasma) since the kink perturbation introduced by the RMPs dominates the displacement. Only after subtracting the kink response of the plasma, calculated with the VMEC code that has previously been shown to yield good agreement with the experiment, can the phase jump be detected at the corresponding rational surface in the plasma (in AUG, using an $n = 2$ RMP pattern, often the 7/2 surface). An example of such an analysis is shown in figure 2, where the RMP field has been varied to slowly rotate the magnetic island past the ECE diagnostic as indicated in the upper left panel.

An important, but still unexplained, observation is the absence of full ELM suppression using RMPs above a certain H or He concentration in mixed H/D ($n_H/n_e \sim 0.4$) [12] and He/D ($n_{He}/n_e \sim 0.2$) plasmas. In these experiments, the conditions for full ELM suppression in D, i.e. low enough edge density and resonant q_{edge}, are fulfilled and the typical density pump-out is observed, but ELMs are only mitigated, not suppressed. This may indicate that the difference is due to a change of the 3-D MHD stability, since pedestal n_e and T_e are well within the range of complete ELM suppression observed in D plasmas.

Concerning naturally ELM-free scenarios, the full variety of scenarios studied in AUG was presented at the previous IAEA FEC [13]. Recent studies focused especially on the regimes that are compatible with a radiative divertor solution,

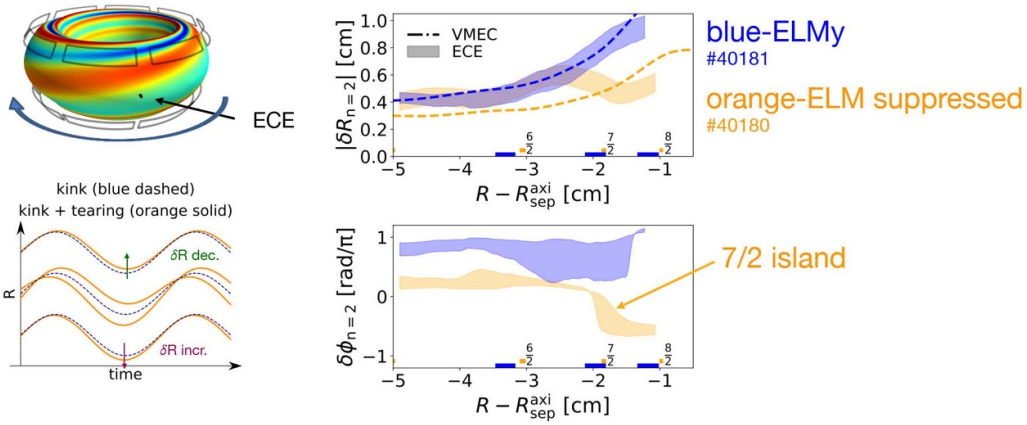

Figure 2. Detection of a magnetic island in the pedestal in an RMP ELM suppressed AUG discharge: the ideal kink response from VMEC is subtracted from the perturbation of the flux surfaces to model the ECE emission. The remaining perturbation shows a phase jump at the $q = 7/2$ surface, indicative of the island, for an RMP ELM suppressed discharge while such a phase jump is not detected in an ELMy H-mode with RMPs applied.

i.e. those that can be run in AUG at high separatrix density and high heating power.

A promising candidate that fulfills these conditions is the quasi continuous exhaust (QCE) regime, in which type I ELMs are replaced by filamentary edge transport, while maintaining good confinement at high density. According to linear and nonlinear MHD modelling, high-n ballooning instabilities soften the pressure gradient at the pedestal foot, moving it away from the peeling-ballooning instability threshold [14, 15]. This is shown in figure 3 for three example discharges. The QCE phases, dubbed 'small ELMs' in the left panel of figure 3, can be seen in the left panel. These coincide with the phases in which the pedestal foot is unstable to ideal infinite-n ballooning modes, as shown in the right panel of figure 3, which shows a contour plot of F_{marg}, the ratio of the ideal limit to the actual pressure gradient. In these phases, ELMs are replaced by the filamentary transport. It has been shown before that, concomitantly, the SOL power fall-off length increases strongly [16]. It can also be seen in figure 3 that higher q_{95} operation eases access to the QCE regime, but when extrapolating to ITER, QCE should be accessible also at low q_{95}. An overview of the parameter range in which the QCE regime can be accessed in AUG can be found in [17]. QCE has recently also been established on JET, including D-T operation at ITER relevant q_{95}, in qualitative agreement with the physics picture described above.

Another ELM-free regime studied recently in AUG is the enhanced D-alpha (EDA) H-mode (first seen on Alcator C-Mod [18]), which occurs at lower separatrix density than the QCE regime [19]. Here, enhanced pedestal transport is ascribed to a Quasi-Coherent Mode (QCM). The EDA operational window has been increased significantly in terms of heating power, applying impurity seeding to keep the separatrix power in the appropriate window, also under ITER baseline conditions. A detailed analysis of the QCM revealed that it also occurs in the QCE regime, with the spectral width becoming broader. The transition between EDA and QCE when increasing the density is rather continuous, indicating the underlying physics could be very similar. The QCM itself was found to be localized at the pedestal foot ($\rho_{\mathrm{pol}} \sim 0.99$), has a poloidal wave number in the range $k_\theta\ \rho_s \sim 0.025$–$0.075$ and propagates in the ion diamagnetic drift direction at $\omega \approx 0.5\ \omega_{i,\mathrm{dia}}$ in the plasma frame [20]. These findings are consistent with the interpretation as a high-n ballooning mode.

Finally, ELMs are also reliably observed to be absent in the X-point radiator (XPR) regime described in more detail in section 4 if the maximum of the radiating zone is located on closed flux surfaces at a certain distance above the X-point (7 cm in AUG). The suppression is possibly due to a softening of the pressure gradient at the pedestal foot, but further analysis is needed to confirm this picture.

3. Transport physics

Experimental studies of the L–H transition support the picture of the well of the radial electric field E_r playing a key role for the transition. It was shown that with favourable drift (ion grad B drift towards the divertor), the E_r minimum at the transition has the same value for a range of densities, heating methods, magnetic fields and when changing the hydrogen isotope. This holds also for the H–L back-transition. However, the E_r minimum is different with reversed ∇B drift, indicating different physics at play [21]. On the modelling side, nonlinear, local GENE simulations of the L-mode edge in power scans approaching the L–H transition reproduce very well the experimentally observed steepening of the pressure and radial electric field gradient [22]. In order to match the experimental results, both electromagnetic effects and E_r shear must be included in the gyrokinetic modelling.

A main aim of core transport studies on AUG is to develop first-principles based full radius modelling capability using reduced models that describe energy and particle confinement at least as well as the usual scaling laws, but allow for more

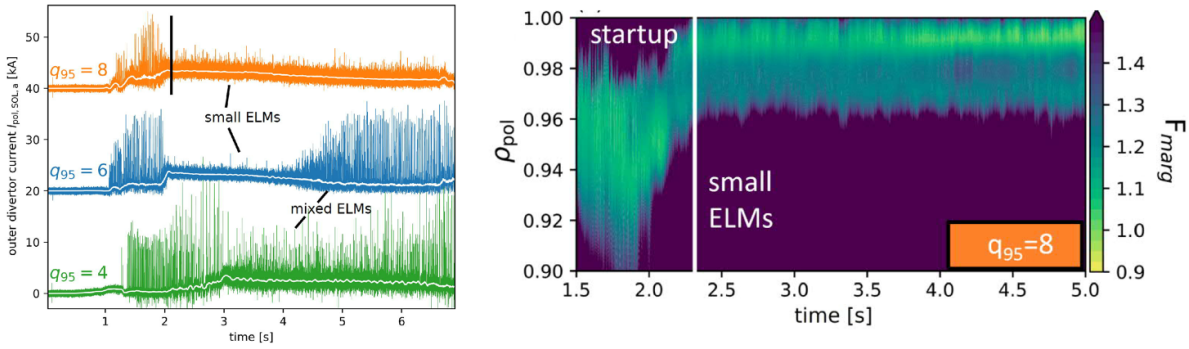

Figure 3. QCE mode on AUG: time traces of the divertor shunt current indicating ELM crashes clearly show the absence of large ELMs in the QCE phase (left). These phases coincide with the pedestal pressure gradient exceeding the ideal ballooning marginal stability at the pedestal foot ($F_{\mathrm{marg}} < 1$ in the right panel for the time point indicated by the vertical line in the left panel).

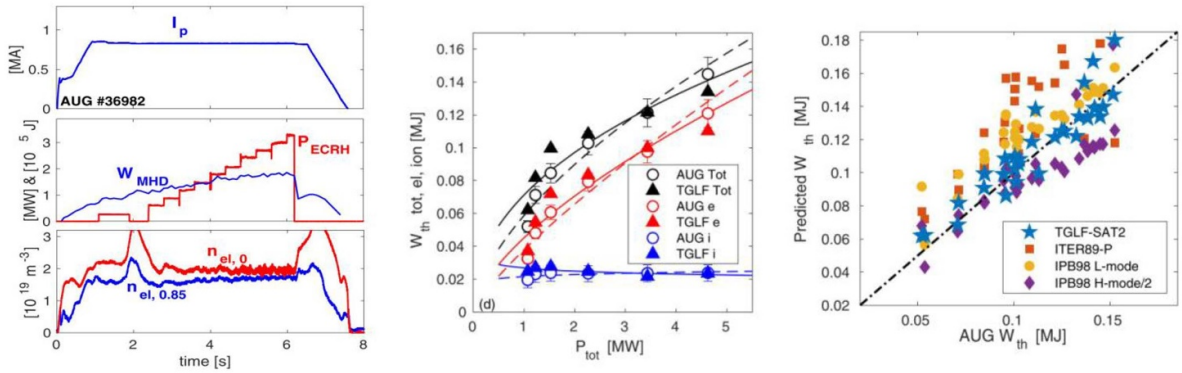

Figure 4. Full radius modelling of L-mode transport in AUG using TGLF: the stored energy (middle figure) in an experimental ECRH power scan (left figure) is reproduced very well, including the (varying) split between electrons and ions. The right figure shows that the model outperforms several scaling laws.

robust extrapolation to ITER and DEMO, due to their physics-based nature. Using the latest version of the TGLF quasilinear transport model in ASTRA, it was, for the first time, possible to model an L-mode parameter scan of AUG discharges over the full radius, prescribing only the sources and the separatrix temperature and density, where $T_{e,\mathrm{sep}}$ is taken from the 2-point model, $T_{i,\mathrm{sep}}$ is set to 1.5 $T_{e,\mathrm{sep}}$, and $n_{e,\mathrm{sep}}$ is assumed to be $n_{e,\mathrm{sep}} = 0.3 <n_e>_{\mathrm{vol}}$ [23]. Figure 4 shows an example for an ECRH power scan as well as a comparison of the model to two L-mode scaling laws, and for reference, also half of the IPB98 H-mode scaling law.

It is found that the main experimental features of L-mode transport, such as strong I_p dependence, confinement increase with increasing density and power degradation, are described very well, with the stored energy from TGLF-ASTRA matching the experimental values better than L-mode scaling laws. This allows a physics interpretation of the individual dependencies [24]. For example, the improvement of energy confinement with plasma current at fixed toroidal field B_t can be traced back to increased *ExB* stabilisation with the variation of the safety factor. Thus, if B_t is increased at constant current, the change in q will deteriorate confinement, largely offsetting the beneficial effect of increased B_t due to the gyro-Bohm scaling. This interplay explains the weak overall scaling of confinement with B_t.

Concerning full radius integrated modelling of H-mode discharges, the successful IMEP scheme [25] which combines a pedestal model based on peeling-ballooning stability and a critical gradient model for electron temperature in the pedestal was extended to describe the pedestal of Alcator C-Mod and JET discharges with good accuracy. While the original, dimensional critical pedestal-temperature-gradient, which describes the AUG pedestal quite well, could not predict the pedestal characteristics of C-Mod and JET, a normalisation to the major radius of the machine (representative of the toroidal field curvature), leads to excellent agreement [26].

A new framework to study momentum transport was developed based on NBI modulation experiments [27]. By fitting the spatio-temporal variation of the rotation profiles in such experiments, it is possible to separate momentum diffusivity, convection, and residual stress in H-mode plasmas. Here, it is assumed that all three components obtain their time dependency mainly from a scaling with the experimentally determined ion heat diffusivity, which is taken as a proxy for the perturbed turbulence intensity, to compensate for the cross-channel perturbation induced by the beam modulation. It can be seen in figure 5 that with this Ansatz, the experimental data can be fitted very well (upper row of figure 5). Moreover, a comparison of the resulting diffusivity and pinch (lower row of figure 5), normalised to the ion heat conductivity, shows good

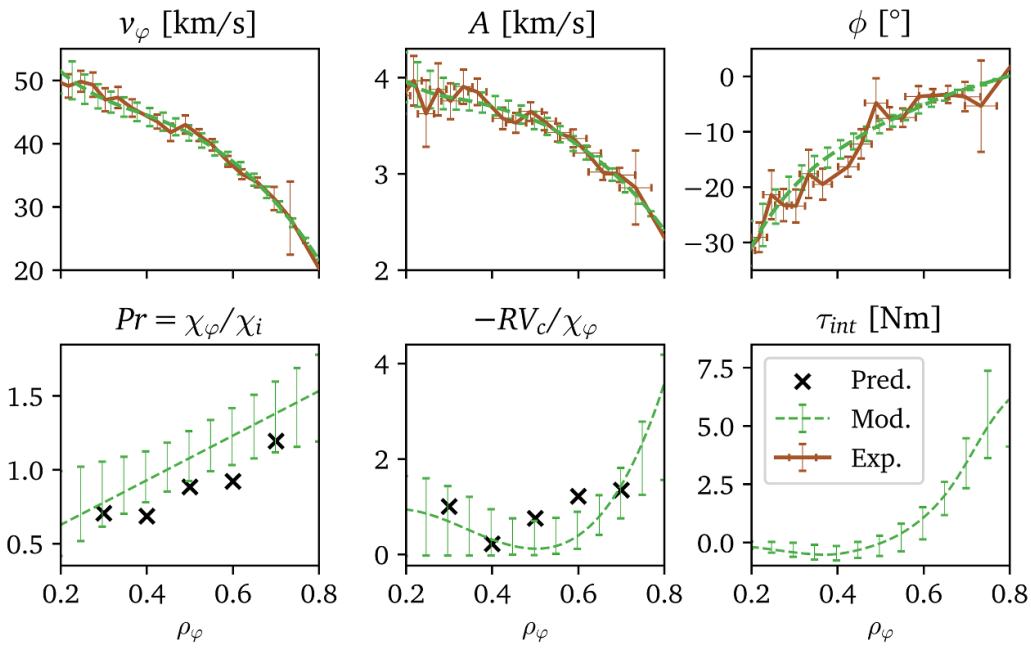

Figure 5. Analysis of momentum transport in NBI torque modulation experiments. Fitting simultaneously the steady-state, amplitude and phase profiles of the rotation (upper row) allows to separate the normalised diffusivity and pinch as well as the local intrinsic torque contributions (lower row). The black crosses indicate predictions by the gyrokinetic code GKW.

agreement with gyrokinetic predictions by the GKW code. The study also shows that it is important to include the time dependent local intrinsic torque, shown as well in the lower row of figure 5, to reproduce the experimental data to high accuracy and to match the gyrokinetic prediction. An analysis of a pair of H and D discharges showed little influence of the isotope on the normalised momentum transport coefficients, agreeing with gyrokinetic calculations [28]. The new framework is being used to systematically validate gyrokinetic predictions and to study parameter dependencies of the intrinsic torque.

4. Integrated exhaust scenarios

Establishing integrated solutions for power and particle exhaust that combine benign target loads, efficient pumping of fuel and impurity particles, and acceptable impact on the core plasma performance has been a major subject of research on AUG. These studies make full use of the ample heating power available, in combination with feedback-controlled impurity seeding using different gases to enhance radiative losses from both the confined plasma as well as SOL and divertor region. Previously, robust control of the XPR, a cold and dense region with high radiative losses, localised on closed flux surfaces close to the X-point had been demonstrated [29]. More recently, an analytical model for the XPR, based on particle and energy balance, has been developed [30]. This model describes successfully the access conditions to the XPR regime as well as the transition from a stable XPR to an unstable MARFE, which sets the limitation on the operational space of the XPR regime. SOLPS calculations show very good agreement with the model [31]. Since in the XPR regime, a total radiated power of up to 95% of the heating power can be stably achieved, it is deemed an attractive solution for ITER and DEMO due to the more homogeneous spreading of the power compared to radiative divertor solutions.

Based on the XPR regime, a new exhaust configuration with the X-point very close to the target plate was established (see figure 6). In this compact radiative divertor (CRD) regime [32], the divertor can be stably detached while maintaining good confinement. In this configuration, the flux expansion is large (e.g. more than 50 in the right panel of figure 6) and, despite the very shallow field line incidence, no overheating of leading edges is observed at high heating power (up to 15 MW). Although the magnetic divertor is far away from baffling structures, neutral density can be quite high, allowing for efficient pumping. This is explained by the trapping of neutrals in the wide plasma fan observed in SOLPS modelling of this configuration [33]. Similar to the XPR regime, there are no large ELMs (see also section 4). This regime might be very attractive for future reactor-grade devices, as it offers the possibility to maximise the plasma volume and breeding zone. In future reactors, such regimes must be robust against reattachment [34]. For the CRD, heat pulses of 75% of the applied heating power could be compensated by the active XPR control. Additionally, the injection of impurity doped pellets is a potential actuator to quickly counteract the risk of reattachment. This was demonstrated in AUG, with doped pellets resulting in a more rapid increase of radiated power with higher radiation efficiency compared to impurity seeding by gas puff [35].

Efficient particle exhaust is another important function of the divertor. The exhaust of He in AUG was characterized

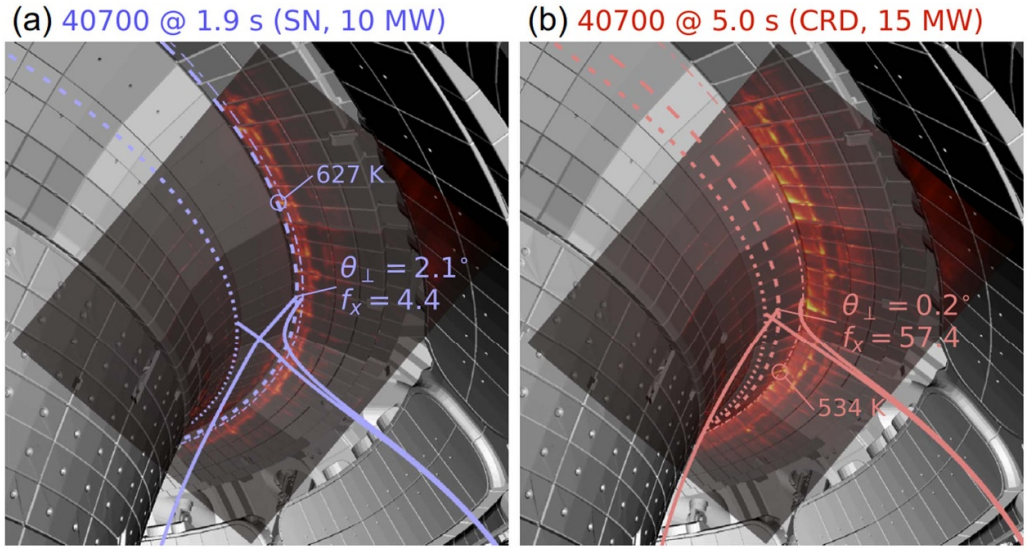

Figure 6. CRD experiments in AUG: starting from an upper single null configuration (left) the plasma is shifted closer to the target plates, strongly increasing the flux expansion f_x. In the CRD configuration (right), the total heating power of 15 MW is exhausted without overloading leading edges in the wetted area, despite the low field line incidence angle of 0.2 degrees.

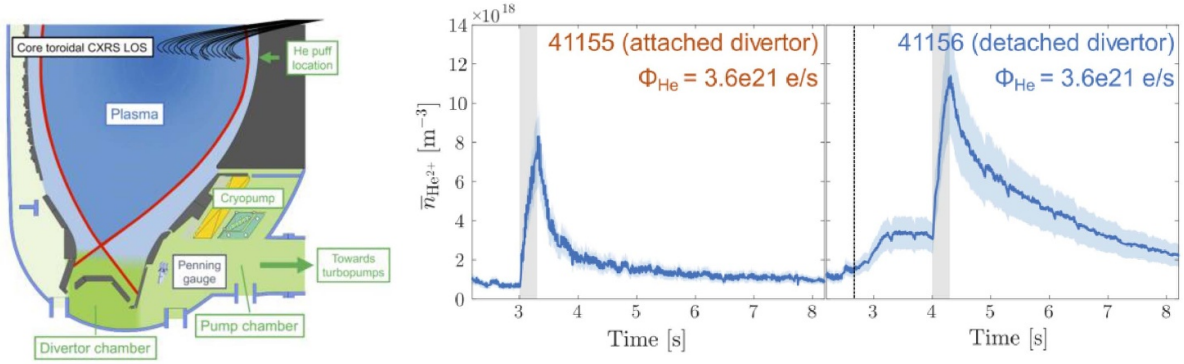

Figure 7. Study of He pumping in AUG: simultaneous measurement of the core He density by CXRS and the neutral density in the pump chamber using a Penning gauge allows to study the enrichment of He. The left panel shows the experimental setup, the right panels show the decay of the core He density after a He gas puff in attached and detached divertor conditions, indicating that the He pumping is less efficient in detached conditions.

in detail by measuring both the He concentration in the core plasma as well as neutral He in the pump duct (see left panel of figure 7). Applying a He gas puff to the plasma, the decay of the core concentration can be measured (right panels of figure 7). A complete description of the He inventory was set up [36], including the core particle confinement, the He recycling, the trapping in the main chamber and the divertor wall elements and, finally, the pumping of neutrals. Separation of the different terms by time dependent modelling is important to characterize the influence of wall conditioning and isolate it from the physics that would determine the He pumping in steady state, as will occur in a fusion reactor. Applying this analysis to experiments like the one shown in figure 7, it is seen that under detached conditions, He removal is indeed slower, attributed to a lower He compression $C_z = n_{z0,\mathrm{div}}/n_{z,\mathrm{main}}$ under these conditions ($n_{z0,\mathrm{div}}$ is the neutral density in the divertor, $n_{z,\mathrm{main}}$ the ion density in the core).

Particle balance studies of recycling impurities showed that their removal is always dominated by the pumping efficiency, emphasizing the importance of the divertor enrichment, $\eta_z = C_z/C_{\mathrm{Deuterium}}$. This quantity has been determined for He, N_2, Ne, Ar and Kr in AUG [37], and it was shown that the main parameter ordering the different species is the ionization energy, leading to values of $\eta > 10$ for Kr and N_2, while He has values below 1. In line with the result quoted above, the study found that under detached divertor conditions, the He enrichment is reduced by a factor of 1.4, while no difference in enrichment was found between standard ELMing H-modes and the EDA/QCE regimes.

5. MHD stability and disruption studies

Concerning MHD stability, experiments validated the recently adopted ITER strategy for error field correction based on the

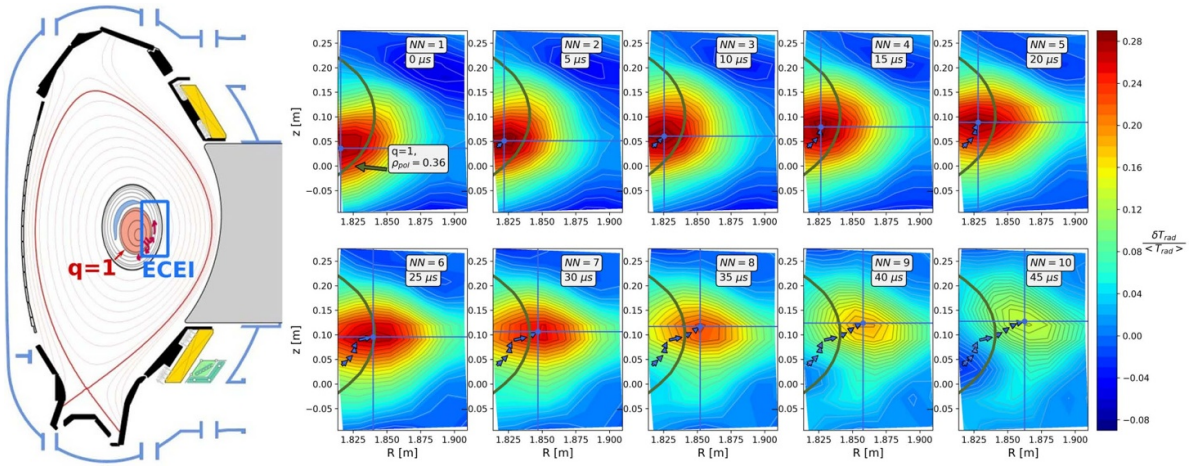

Figure 8. Analysis of sawtooth reconnection using ECE Imaging: the motion of the hot core across the $q = 1$ surface is followed by offset corrected temperature measurements. The radial velocity of the core is directly related to the reconnection rate.

plasma response. If the RMP coil current phasing is chosen to maximise the overlap with the ideal MHD plasma response due to the error field (calculated from a detailed electromagnetic model of the AUG coils and their feeders), the ideal β-limit is highest [38], outperforming other correction strategies based on correcting the vacuum field error field.

Also in the area of MHD stability, detailed measurements of the motion of the hot plasma core during sawtooth reconnection using ECE imaging enabled the study of reconnection rates [39]. An example is shown in figure 8, where the dots and arrows map out the motion of the hot core and show a clear transition from rotation to radial motion between the upper and the lower panel. A comparison with nonlinear 2-fluid MHD modelling [40] showed consistency in both absolute value and parameter scaling of the hot core motion. The reconnection rate is found to increase with T_e, consistent with the predicted importance of finite Larmor radius effects. This indicates that including the pressure term and electron inertia in the parallel Ohm's law is key to resolving the usual discrepancies when applying a simple Kadomtsev model, which for the cases studied would yield a large discrepancy in absolute value as well as the wrong parameter dependence.

Disruption studies were a strong focus of the experimental programme, supported by the SPI system, which was installed in 2022 and financed through a collaboration with ITER Organisation. This system allows different shatter head geometries to be tested, resulting in a variation in the pellet shard size distribution independent of the injection velocity. A comprehensive characterisation under laboratory conditions was performed, yielding quantitative information on the dependence of the shard size distribution and its dependence on the injection speed [41]. These were found to exhibit discrepancies when compared to the predictions of the model presented in [42], indicating the need to refine the theory. This is important since the shard size and velocity distribution are key inputs to nonlinear MHD simulations aimed at understanding the quenching process initiated by SPI [43].

In a series of experiments, SPI was applied to shut down AUG plasmas [44, 45]. An important experimental knob is the pellet composition, which can be of varying deuterium/neon fraction. Higher Ne fractions lead to an increase in radiation and a faster current quench. To date, optimum plasma termination was achieved with a D-pellet for pre-cooling, followed by a Ne (doped) pellet to rapidly reduce the plasma current. Tailoring the radiation fraction and the current quench time by multiple injections will be an important tool to simultaneously fullfil the ITER shutdown requirements such as limiting the forces and avoiding excessive runaway generation.

Progress was also made in understanding the reduction of forces by injecting impurities via massive gas injection MGI through a full nonlinear MHD simulation of the process, including the VDE following the thermal quench that determines these forces [46].

As another focus of disruption studies, the DCS was equipped with new control capabilities and was used to study safe tokamak operation close to the H-mode density limit (HDL). The aim of the studies is to characterise the safe operational space in a parameter space accessible to real-time evaluation and to move the discharge back into this region once the boundary of the safe space is crossed. A characterisation of the plasma state in terms of edge density and confinement quality allowed safe navigation of the discharge close to the HDL [47]. This scheme was successfully transferred to TCV [48], and the operational space at AUG was determined for variations of different parameters, such as triangularity and the heating and fuelling method [49]. Since the HDL is often initiated by the formation of a MARFE, these studies are directly linked to the characterisation of the XPR and its stability described in the previous section.

Figure 9 shows how the DCS is used to conduct explorations of the operational space: the experiment shown explores the impact of heating power on the HDL [50]. In order to probe this, the gas flux is ramped strongly (trace 'D_{tot}' in the left panel of figure 9) until a MARFE is detected by the XPR crossing a bolometer sightline above the X-point (trace 'XPR position'). This triggers the switch from the HDL segment of the discharge programme to a recovery segment, in which the gas flux is reduced and additional heating power is applied,

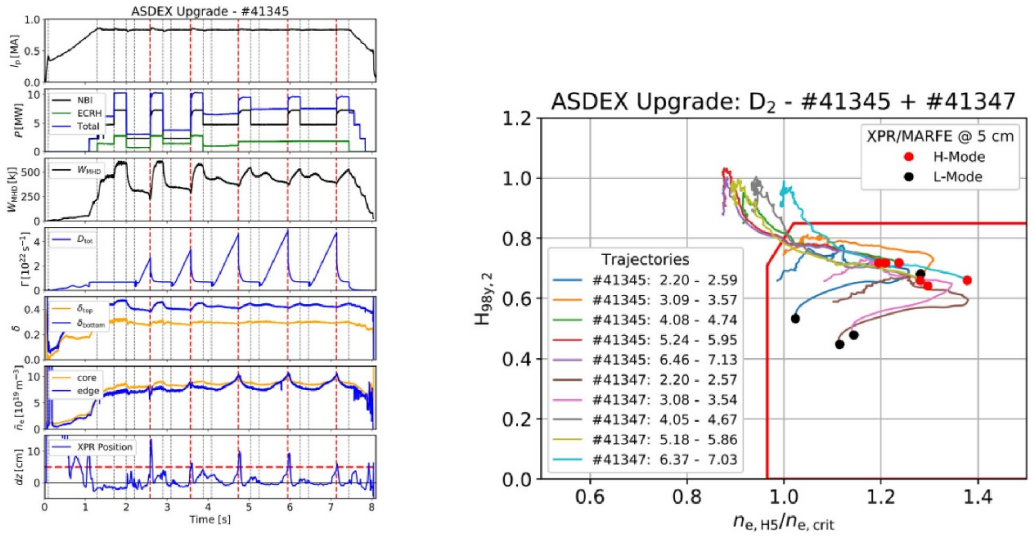

Figure 9. Experiments probing the safe operational space: in each segment of the discharge, the density is increased by gas puff (trace labelled 'D_{tot}' in the left panel) until a MARFE is detected, which leads to the DCS switching to a recovery segment. Then, the gas puff is increased again, at different heating power. The trajectories of such experiments are shown in the right panel, indicating how they can be characterised in the space of normalised confinement versus normalised edge density.

reducing the MARFE to a stable XPR. Then, the next HDL segment is activated, probing the MARFE stability at a different (higher) total heating power. The experiment shown lead to 5 different explorations of the operational space in a single discharge without a disruption, while a feedforward procedure would have taken 5 disruptive discharges. It therefore outlines a procedure how the operational limits can be probed in future experiments without disruptive termination. The right panel of figure 9 shows the trajectories of this discharge and others in the normalised space mentioned above. The HL transition can be recognised by the decrease in edge density, while maintaining the discharge in the 'safe' space outlined by the red box will guarantee that the discharge stays away from that limit.

6. Integrated operation scenarios

The development of integrated operation scenarios focuses on both the ITER baseline (low q_{95} H-mode) and advanced tokamak (AT) scenarios. Concerning the latter, both hybrid (central q-value just above 1) and elevated central q-profiles have been studied.

For the ITER baseline scenario, studies focused on understanding the reduction of the H-factor $H_{98(y,2)}$ observed at high density/Greenwald fraction [51] shown in figure 10.

In AUG, the high-density regime is related to high collisionality, and the density profiles are hence flat due to the reduction of turbulent inward pinch with increasing collisionality [51]. This has been identified as the main correlation with the reduction in H98(y,2), as can be seen in the middle panel of figure 10. This is different to other regimes, where in AUG, confinement degradation at high density is often attributed to a deterioration of the pedestal, as e.g. discussed below for AT scenarios. The H20 scaling [52], on the other hand, captures this effect, as can be seen in the right panel of figure 10. We note, however, that for ITER, a significant density peaking is predicted by TGLF [53], putting the operational point close to the low-density AUG operational space. This finding emphasizes the need for physics based full radius modelling rather than application of scaling laws when extrapolating to future devices, as outlined in section 3 above.

For AT scenarios, the large variation in H_{98} observed experimentally, ranging between H = 0.85 and H = 1.35, was traced back to a variation of the separatrix density [54] that influences the pedestal height: higher separatrix density moves the region of steepest pedestal density gradient towards the separatrix, reducing the MHD stability, as shown previously for standard H-modes [55]. This knowledge has been used to optimise the confinement of AT discharges. Concerning the current ramp-up phase in AT scenarios, predictive modelling has been set up to guide the access to the target current profile by employing the actuators for current drive (NBCD and ECCD). Predicting the electron temperature profile evolution with a mixed Bohm/gyro–Bohm model, the ASTRA code could successfully predict the timing of the actuators to access targeted elevated q-profiles with minimum flux consumption [56, 57]. Studies using the RAPTOR code to achieve this goal with a nonlinear optimisation algorithm also showed very promising results [57]. These procedures will be very beneficial to minimise ramp-up time and flux consumption in future large devices with a very long current redistribution time.

Using these tools, two main lines were followed, namely the hybrid scenario with central q close to 1, but no sawteeth [58], and a scenario with an elevated q-profile with $q_{\min} > 1.5$ [56]. In the hybrid scenario, flux pumping provides a redistribution of the central current density by a central MHD mode to keep $q > 1$, allowing even for central ECCD to drive part of the current with good CD efficiency. An example of a fully non-inductive discharge is shown in figure 11. In the left panel,

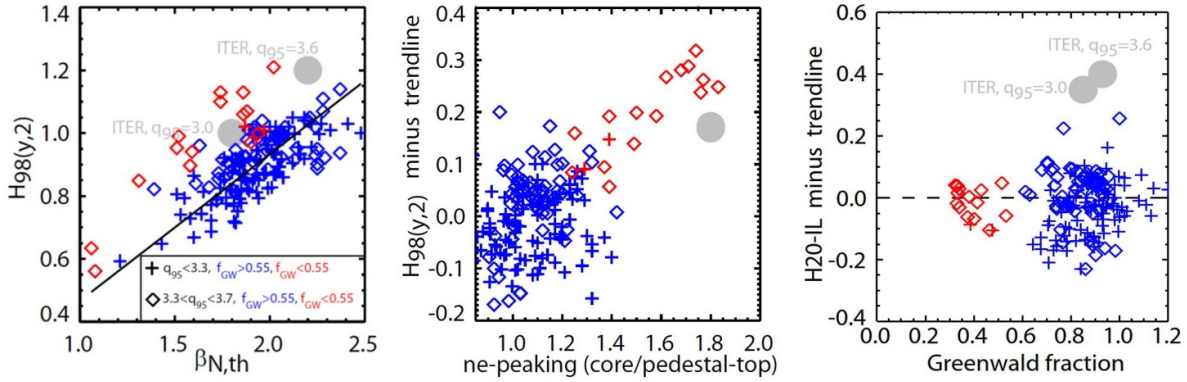

Figure 10. Confinement studies in the ITER baseline scenario in AUG: at high Greenwald fraction (blue points), the normalised confinement $H_{98(y,2)}$ (middle panel) is below unity. This is due to the reduced density peaking compared to the low Greenwald fraction cases (red points). The H20 scaling (right panel), however, captures this trend. The ITER operational point (grey dot) is predicted to be in the regime of high density peaking.

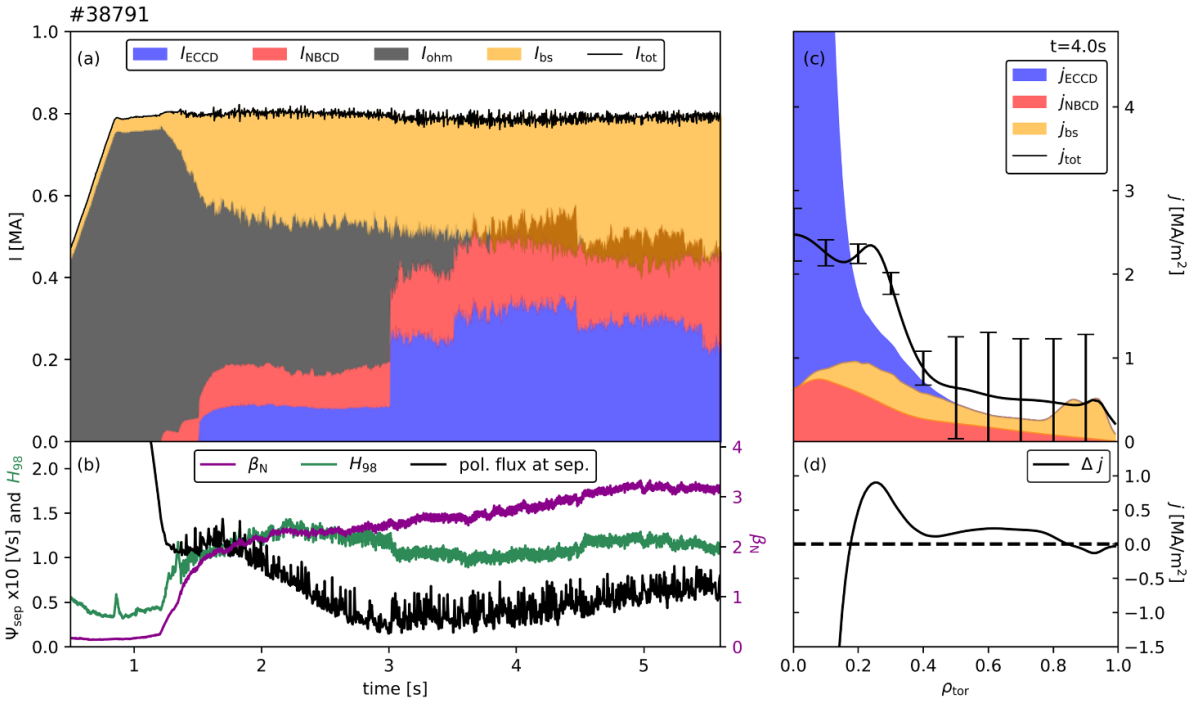

Figure 11. Example of a fully noninductive discharge scenario in the hybrid regime. About 50% of the current is due to the bootstrap current, the rest is driven by NBCD and ECCD (left panel). The increase of poloidal flux at the separatrix indicates a slight 'overdrive', i.e. recharging of the transformer. The current profile composition is shown on the right. The inconsistency with conventional modelling (lower right panel) indicates the effect of flux pumping at the $q = 1$ surface.

one can see that stationary conditions are achieved with the H-factor exceeding 1 and β_N higher than 3. The current composition indicates that up to 50% is driven by bootstrap current, with the other 50% being supplied by NBCD and ECCD. The brown region starting at 4 s indicates slight overdrive, as can also be seen by the increase of poloidal flux at the boundary in figure 11(*b*) (indicating a negative loop voltage). From figure 11(*c*), it can be seen that for the current density inferred by time dependent equilibrium reconstruction incorporating kinetic constraints [59], there is a good fit with the driven current in the outer part of the plasma, whereas there is a clear inconsistency further inward. The difference, Δj in figure 11(*d*), is consistent with the flux pumping redistribution of the current profile mentioned above, which can be explained by a stationary central quasi-interchange (1,1) mode whose flow pattern generates a nonlinear toroidal component of the dynamo loop voltage [60].

As mentioned above, a second AT scenario studied in AUG is based on an elevated ($q_{\min} > 1.5$) current profile. This has been established successfully using cental ctr-ECCD. While it can, in principle, have a higher bootstrap current efficiency due to the elevated central q ($j_{bs} \sim \nabla p\, q$), it has been found experimentally to exhibit a lower β-limit of $\beta_{N,max} \approx 2.8$ as opposed to $\beta_{N,max} \approx 3.3$ in the hybrid scenario. This is in line

with the expected no-wall β-limit (in AUG, the wall is situated quite far away from the plasma so that it is not expected to play a strong stabilising role [61]). A detailed comparison of these two scenarios will be conducted in the near future.

Negative triangularity (δ) configurations were studied for the first time in AUG [62], limited in shape by the constraint to fit the divertor legs into the existing divertor structure. Hence, high power could only be applied to configurations with upper $\delta = -0.2$ and average δ close to zero. In the favourable ∇B-drift direction, H-mode was accessed easily in this configuration. With unfavourable drift direction, using ECRH only, improved L-mode confinement ($H_{98} \sim 1$) was found, which can also occur in low current positive triangularity discharges, albeit not at this level ($H_{98} \leqslant 0.8$). Conversely, in power scans up to 13 MW with dominant NBI, confinement was close to usual L-mode levels, exhibiting a pronounced power degradation. The negative delta shape would have to be improved to more negative values in order to understand if improved L-mode confinement, as is found in TCV [63] and DIII-D [64] can also be established at higher heating power in AUG.

7. Summary and conclusions

The results presented here show substantial progress in understanding the plasma physics of tokamak fusion reactors. In the area of pedestal physics, RMP ELM mitigation was found to be consistent with a reduction of the linear peeling-ballooning stability threshold due to the helical deformation of the plasma. In contrast, ELM suppression by RMPs is ascribed to an increased pedestal transport that keeps the plasma away from this boundary. Candidates for this increased transport are locally enhanced turbulence and a locked magnetic island in the pedestal. The EDA/QCE regime has been established as a promising ELM-free scenario in which the pressure gradient at the pedestal foot is reduced by a quasi-coherent mode, consistent with local violation of the ideal, high-n, ballooning mode stability limit there. In the area of transport, progress has been made towards full radius modelling of both L- and H-modes. These models now outperform the usual scaling laws in predicting energy confinement on AUG. A new analysis method for momentum transport points out the importance of including time dependent transport coefficients and the intrinsic torque in the analysis and provides the basis for parametric studies. Access to the XPR regime, a cold and dense strongly radiative zone on closed flux surfaces, was understood in terms of an analytical model, confirmed by SOLPS calculations. Moving the XPR close the target established a new detached divertor concept, the CRD, in which the exhaust power is radiated before reaching the target without limitation by shallow field line angles. Pumping of non-recycling impurities, including He, was studied in detail, showing that the divertor enrichment of the impurity mainly depends on its ionisation energy. Detailed studies of sawtooth crashes showed good agreement with nonlinear 2-fluid simulations, indicating that the fast reconnection is adequately described by including the pressure gradient and electron inertia in Ohm's law. In the area of disruption mitigation and avoidance, a newly installed SPI system allowed the study of the plasma shutdown with varying pellet impurity admixtures, demonstrating the possibility to tailor the current quench rate. Disruption avoidance was studied for the HDL, mapping out the safe operational space with a newly developed active feedback control method. The role of density peaking in the confinement of the ITER baseline scenario was clarified, highlighting again the need to move from scaling laws to physics based models. Concerning advanced scenarios, access to target q-profiles was guided by a newly developed modelling approach and the conditions for achieving good confinement were clarified. Based on this, advanced scenarios of the hybrid type as well as with elevated q-profile were established on AUG.

Concerning future directions, AUG entered a shutdown scheduled until September 2024 for the installation of the new upper divertor with in-vessel coils that will allow the study of advanced divertor physics in a variety of configurations. In particular, various configurations with enhanced flux expansion in conjunction with the new flat divertor tiles will allow to study benefit and limits of this technique. Also, the shaping capabilities will be improved due to enhancements of the PF coil current supply, increasing the flexibility to study the impact of shape on plasma properties, such its role in reliably achieving the QCE regime. Furthermore, an initiative has been started to augment the diagnostic capabilities to better understand the physics of disruptions and their mitigation. These extensions will further improve our capability to establish first principles understanding of fusion plasma physics, which is needed in order to safely extrapolate from present day devices to reactors. Together with other tokamaks worldwide, operational experience gained on AUG will directly inform ITER operation, aiming to optimise the path to $Q = 10$ once it has started operation.

Acknowledgments

This work has been carried out within the framework of the EUROfusion Consortium, funded by the European Union via the Euratom Research and Training Programme (Grant Agreement No. 101052200—EUROfusion). The views and opinions expressed are, however, those of the author(s) only and do not necessarily reflect those of the EU or the EC. Neither the EU nor the EC can be held responsible for them.

References

[1] The ASDEX Upgrade Team 2003 ASDEX Upgrade Special Issue *Fusion Sci. Technol.* **44**
[2] Fable E. *et al* 2022 The modeling of a tokamak plasma discharge, from first principles to a flight simulator *Plasma Phys. Control. Fusion* **64** 044002
[3] Joffrin E. *et al* 2024 Overview of the EUROfusion tokamak exploitation programme in support of ITER and DEMO *Nucl. fusion* **64** 112018

[4] Dibon M. *et al* 2023 Design of the shattered pellet injection system for ASDEX Upgrade *Rev. Sci. Instrum.* **94** 043504
[5] Hopf C. *et al* 2024 Decoupling beam power and beam energy on ASDEX Upgrade NBI with an in-situ variable extraction gap system *Nucl. Fusion* **64** 096017
[6] Lunt T., Zohm H., Herrmann A., Kallenbach A., Dunne M., Feng Y., Neu R. and Wischmeier M. 2017 Design of an alternative upper divertor in ASDEX Upgrade supported by EMC3-eirene simulations *Nucl. Mater. Energy* **12** 1037
[7] Herrmann A. *et al* 2019 A new upper divertor with internal coils for ASDEX Upgrade—status of the project *Fusion Eng. Des.* **146A** 920
[8] Suttrop W. *et al* 2018 Experimental conditions to suppress edge localised modes by magnetic perturbations in the ASDEX Upgrade tokamak *Nucl. Fusion* **58** 096031
[9] Puchmayr J. *et al* 2024 Effect of symmetry-breaking on the MHD edge stability limit of tokamak plasmas *Nucl. Fusion* **64** 086013
[10] Leuthold N. *et al* 2023 Turbulence characterization during the suppression of edge-localized modes by magnetic perturbations on ASDEX Upgrade *Nucl. Fusion* **63** 046014
[11] Willensdorfer M. *et al* 2023 Magnetic islands in 3D tokamak plasmas during the suppression of filamentary eruptions (https://doi.org/10.21203/rs.3.rs-3286107/v1)
[12] Leuthold N. *et al* 2024 Progress towards edge-localized mode suppression via magnetic perturbations in hydrogen plasmas *Nucl. Fusion* **64** 026017
[13] Stroth U. *et al* 2022 Progress from ASDEX Upgrade experiments in preparing the physics basis of ITER operation and DEMO scenario development *Nucl. Fusion* **62** 042006
[14] HARRER G. *et al* 2022 Quasicontinuous exhaust scenario for a fusion reactor: the renaissance of small edge localized modes *Phys. Rev. Lett.* **129** 165001
[15] Cathey A. *et al* 2024 Non-linear MHD investigations of high-confinement regimes without type-I ELMs in ASDEX Upgrade and JT-60SA *Nucl. Fusion* **64** 096003
[16] Faitsch M., Eich T., Harrer G.F., Wolfrum E., Brida D., David P., Griener M. and Stroth U. 2021 Broadening of the power fall-off length in a high density, high confinement H-mode regime in ASDEX Upgrade *Nucl. Mater. Energy* **26** 100890
[17] Faitsch M. *et al* 2023 Analysis and expansion of the quasi-continuous exhaust (QCE) regime in ASDEX Upgrade *Nucl. Fusion* **63** 076013
[18] Greenwald M. *et al* 1999 Characterization of enhanced D_α high-confinement modes in Alcator C-Mod *Phys. Plasmas* **6** 1943
[19] GIL L. *et al* 2020 Stationary ELM-free H-modes in ASDEX Upgrade *Nucl. Fusion* **60** 054003
[20] Kalis J. *et al* 2024 Experimental characterization of the quasi-coherent mode in EDA H-mode and QCE scenarios at ASDEX Upgrade *Nucl. Fusion* **64** 016038
[21] Plank U. *et al* 2023 Experimental study of the role of the edge radial electric field on the access to H-mode at ASDEX Upgrade *Phys. Plasmas* **30** 42513
[22] Bonanomi N. *et al* 2022 From L-mode to the L-H transition, experiments on ASDEX Upgrade, gyrokinetic simulations and full-radius transport modelling *48th EPS Conf. on Plasma Physics* (*Online*, *27 June–1 July 2022*) (available at: http://ocs.ciemat.es/EPS2022PAP/html/)
[23] Angioni C. *et al* 2022 Confinement properties of L-mode plasmas in ASDEX Upgrade and full-radius predictions of the TGLF transport model *Nucl. Fusion* **62** 066015
[24] Angioni C., Bonanomi N., Fable E., Schneider P.A., Tardini G., Luda T. and Staebler G.M. 2023 The dependence of tokamak L-mode confinement on magnetic field and plasma size, from a magnetic field scan experiment at ASDEX Upgrade to full-radius modelling and fusion reactor predictions *Nucl. Fusion* **63** 056005
[25] Luda T. *et al* 2021 Validation of a full-plasma integrated modeling approach on ASDEX Upgrade *Nucl. Fusion* **61** 126048
[26] Luda T. *et al* 2023 Validation of IMEP on Alcator C-Mod and JET-ILW ELMy H-mode plasmas *Plasma Phys. Control. Fusion* **65** 034001
[27] Zimmermann C.F.B. *et al* 2023 Experimental determination of the three components of toroidal momentum transport in the core of a tokamak plasma *Nucl. Fusion* **63** 124003
[28] Zimmermann C.F.B. *et al* 2023 Comparison of momentum transport in matched hydrogen and deuterium H-mode plasmas in ASDEX Upgrade *Nucl. Fusion* **63** 124006
[29] Bernert M. *et al* 2021 X-point radiation, its control and an ELM suppressed radiating regime at the ASDEX Upgrade tokamak *Nucl. Fusion* **61** 024001
[30] Stroth U. *et al* 2022 Model for access and stability of the X-point radiator and the threshold for MARFEs in tokamak plasmas *Nucl. Fusion* **62** 076008
[31] Pan O. *et al* 2023 SOLPS-ITER simulations of an X-point radiator in ASDEX Upgrade *Nucl. Fusion* **63** 016001
[32] Lunt T., Bernert M., Brida D., David P., Faitsch M., Pan O., Stieglitz D., Stroth U. and Redl A. 2023 Compact radiative divertor experiments at ASDEX Upgrade and their consequences for a reactor *Phys. Rev. Lett.* **130** 145102
[33] PAN O. *et al* 2023 The compact radiative divertor in ASDEX Upgrade and EU-DEMO, experiments & simulation *Preprint: IAEA Fusion Energy Conf. (London, 16–21 October 2023)* CN-316/2506
[34] Henderson S.S. *et al* 2023 Divertor detachment and reattachment with mixed impurity seeding on ASDEX Upgrade *Nucl. Fusion* **63** 086024
[35] Kallenbach A. *et al* 2023 Argon doped pellets for fast and efficient radiative power removal in ASDEX Upgrade *Nucl. Fusion* **62** 106013
[36] Zito A. *et al* 2023 Investigation of helium exhaust dynamics at the ASDEX Upgrade tokamak with full-tungsten wall *Nucl. Fusion* **63** 096027
[37] Kallenbach A. *et al* 2024 Divertor enrichment of recycling impurity species (He, N2, Ne, Ar, Kr) in ASDEX Upgrade H-modes *Nucl. Fusion* **64** 056003
[38] Igochine V., Bonotto M., Gude A., Maraschek M., Pigatto L., Bettini P., Liu Y.Q., Piron L., Voltolina D. and Zohm H. 2023 Plasma effect on error fields correction at high β_N in ASDEX upgrade *Plasma Phys. Control. Fusion* **65** 062001
[39] Samoylov O. *et al* 2022 Magnetic reconnection velocity during sawtooth crashes in ASDEX Upgrade *Nucl. Fusion* **62** 074002
[40] GÜNTER S., Yu Q., Lackner K., Bhattacharjee A. and Huang Y.-M. 2015 Fast sawtooth reconnection at realistic Lundquist numbers *Plasma Phys. Control. Fusion* **57** 014017
[41] Peherstorfer T. 2022 Fragmentation analysis of cryogenic pellets for disruption mitigation *Masters Thesis TU Vienna* (available at: https://arxiv.org/pdf/2209.01024.pdf)
[42] Parks P.B. 2016 Modeling dynamic fracture of cryogenic pellets *Technical report, General Atomics* p 6
[43] Tang W. *et al* 2023 Non-linear shattered pellet injection simulations based on ASDEX Upgrade experiments *Preprint: IAEA Fusion Energy Conf.(London, 16–21 October 2023)* CN-316/2430
[44] Lehnen M. *et al* 2023 Physics basis and technology development for the ITER disruption mitigation system

Preprint: IAEA Fusion Energy Conf. (London, 16–21 October 2023) CN-316/2509
[45] Heinrich P. *et al* 2023 Radiation characteristics of the SPI experiments at ASDEX Upgrade *10th REM, 2023* (available at: https://ft.nephy.chalmers.se/?p=abstract&id=67)
[46] Schwarz N. *et al* 2023 Mechanisms of the global force reduction in disruptions—experimental validation of mitigated and unmitigated VDEs with the MHD code JOREK *Preprint: IAEA Fusion Energy Conf. (London, 16–21 October 2023) CN-316/2518*
[47] Maraschek M. *et al* 2018 Path-oriented early reaction to approaching disruptions in ASDEX Upgrade and TCV in view of the future needs for ITER and DEMO *Plasma Phys. Control. Fusion* **60** 014047
[48] Pau A. *et al* 2022 Controlled avoidance of disruptions in tokamaks: experience and developments in TCV *Talk presented at 48th EPS Conf. on Plasma Physics* (*Virtual*, *27 June 2022–01 May 2022*) (available at: http://ocs.ciemat.es/EPS2022PAP/html/)
[49] Sieglin B. *et al* 2023 Disruption avoidance and investigation of the H-mode density limit in ASDEX Upgrade *Plasma Phys. Control. Fusion* **66** 025004
[50] Pütterich T. *et al* 2021 The ITER baseline scenario at ASDEX Upgrade and TCV *47th EPS Conf. On Plasma Physics* (*Sitges, Spain*, *21–25 June 2021*) (available at: https://epsplasma2020.eu/)
[51] Angioni C., Peeters A.G., Pereverzev G.V., Ryter F. and Tardini G. 2003 Density peaking, anomalous pinch, and collisionality in tokamak plasmas *Phys. Rev. Lett.* **90** 205003
[52] Verdoolage G. *et al* 2021 The updated ITPA global H-mode confinement database: description and analysis *Nucl. Fusion* **61** 076006
[53] Pereverzev G., Angioni C., Peeters A.G. and Zolotukhin O.V. 2005 Theoretical predictions of the density profile in a tokamak reactor *Nucl. Fusion* **54** 221
[54] Silvagni D. *et al* 2024 The impact of divertor neutral pressure on confinement degradation of advanced tokamak scenarios at ASDEX Upgrade *Phys. Plasmas* **31** 022501
[55] Dunne M. *et al* 2017 The role of the density profile in the ASDEX-Upgrade pedestal structure *Plasma Phys. Control. Fusion* **59** 014017
[56] Schramm R. *et al* 2024 Development and application of a predictive model for advanced tokamak scenario design *Nucl. Fusion* **64** 036013
[57] Van Mulders S. *et al* 2024 Inter-discharge optimization for fast, reliable access to ASDEX Upgrade AT scenario *Nucl. Fusion* **64** 026021
[58] Burckhart A. *et al* 2023 Experimental evidence of magnetic flux pumping in ASDEX Upgrade *Nucl. Fusion* **63** 126056
[59] Fischer R. *et al* 2016 Coupling of the flux diffusion equation with the equilibrium reconstruction at ASDEX Upgrade *Fusion Sci. Technol.* **69** 526
[60] Krebs I., Jardin S.C., Günter S., Lackner K., Hoelzl M., Strumberger E. and Ferraro N. 2017 Magnetic flux pumping in 3D nonlinear magnetohydrodynamic simulations *Phys. Plasmas* **24** 102511
[61] Igochine V. *et al* 2017 MHD limits and plasma response in high-beta hybrid operations in ASDEX Upgrade *Nucl. Fusion* **57** 116027
[62] Happel T., Pütterich T., Told D., Dunne M., Fischer R., Hobirk J., McDermott R.M., Plank U. and (the ASDEX Upgrade Team) 2023 Overview of initial negative triangularity plasma studies on the ASDEX Upgrade tokamak *Nucl. Fusion* **63** 016002
[63] Camenen Y. *et al* 2007 Impact of plasma triangularity and collisionality on electron heat transport in TCV L-mode plasmas *Nucl. Fusion* **47** 510
[64] Austin M. *et al* 2019 Achievement of reactor-relevant performance in negative triangularity shape in the DIII-D tokamak *Phys. Rev. Lett.* **122** 115001